Journal of Crystal Growth 604 (2023) 127052

Contents lists available at ScienceDirect

Journal of Crystal Growth

journal homepage: www.elsevier.com/locate/jcrysgro

Hypo-peritectic TRIS–NPG in a stationary temperature gradient: Thermodynamics, grain boundary migration and phase identification

A. Ludwig [a,*], J. Mogeritsch [a], V.T. Witusiewicz [b]

[a] Department Metallurgy, University of Leoben, Franz-Josef-Str. 18, 8700 Leoben, Austria
[b] ACCESS e.V., Intzestr. 5, D-52072 Aachen, Germany

ARTICLE INFO

Communicated by Chennai Guest Editor

Keywords:
A1: Directional Solidification
A1: Optical microscopy
A1: Supersaturated solution
A2: Bridgman technique

ABSTRACT

At a stationary temperature gradient, the grain boundaries comprising residual melt can migrate. Their migration is governed by liquid diffusion and, in multiphase materials, depends highly on the phases present. Therefore, this phenomenon can be used for phase identification if data on metastable extensions of the corresponding phase diagram are available. Thus, we re-optimised the thermodynamic description of Tris(hydroxymethyl) aminomethane-Neopentylglycol (TRIS–NPG), a transparent peritectic alloy often used as a model alloy for metallic solidification, and used the predicted metastable liquidus and solidus curves to evaluate the grain boundary migration observations. As we found temperature gradient zone melting (TGZM) at low temperatures, the presence of the peritectic phase could be excluded even though a near-peritectic alloy had been processed. The liquid diffusivity, as a function of the position/temperature, was estimated from the TGZM velocity measurements. The data suggest that the diffusion coefficient deep in the mush is one order of magnitude smaller than that close to the liquidus temperature. This may be typical for non-dilute alloys, where the concentration of the intergranular liquid changes considerably.

1. Introduction

Extensive research has been conducted on metallic solidification using transparent organic materials that exhibit a high-temperature “plastic crystal” formed by so-called “globular molecules.” These molecules undergo phase transitions from a low temperature-ordered structure (tetragonal, orthorhombic, and monoclinic) to a high-temperature orientationally disordered (face centred cubic (fcc) or body centred cubic (bcc)) phase, referred to as “plastic” or “orientationally disordered crystal (ODIC)”. Based on the reversible breaking of the nearest-neighbour hydrogen bonds in molecular crystals, these solid–solid phase transitions are characterised by a relatively high enthalpy [1]. Hence, as phase change materials, they are of interest for thermal energy storage (TES) applications [2,3]. The low temperature-ordered phases usually appear needle-like as they grow as faceted crystals. Conversely, an ODIC forms cellular and dendritic morphologies that are similar to those of solidifying metals or alloys.

To perform in situ observations of peritectic solidification at low pulling velocities, a Tris(hydroxymethyl)aminomethane–Neopentylglycol (TRIS–NPG) organic system was selected (CAS numbers 77–86-1 and 126–30-7, for TRIS and NPG, respectively). Part of the TRIS–NPG phase diagram relevant to this study is shown in Fig. 1. The phase diagram was experimentally determined by Barrio et al. [4] and recently confirmed by other studies [2,5]. The peritectic invariant reaction, $\alpha + L \leftrightarrow \beta$, is located at $T_p = 410.7$ K and $x_p = 0.51$ mol fraction NPG. The (high temperature) eutectoid invariant reaction, $\alpha \leftrightarrow \beta + O$, is located at $T_{e1} = 392.5$ K and $x_{e1} = 0.43$ mol fraction NPG. Here, α represents the high-temperature plastic TRIS phase (bcc), β refers to the high-temperature plastic NPG phase (fcc), O is the low-temperature faceted TRIS phase (orthorhombic), and L is the liquid phase. The second eutectoid invariant reaction ($\beta \leftrightarrow O + M$, at $T_{e2} = 310.5$ K and $x_{e2} = 0.96$ mol fraction NPG), which involves the monoclinic phase (M) and is promising for TES applications, is not relevant for this study.

Directional solidification experiments applying the Bridgman technique have recently been conducted onboard the International Space Station using several near-peritectic TRIS-NPG alloys [6–8]. To assist this space-based study, ground-based solidification experiments were conducted using thin samples. The results shed light on phenomena that have also been observed in space.

The experimental study presented in this paper uses a hypo-peritectic TRIS–NPG alloy with 0.5 mol fraction NPG and comprises direct observation of melting and grain boundary migration in a given

---

* Corresponding author.
E-mail address: ludwig@unileoben.ac.at (A. Ludwig).

https://doi.org/10.1016/j.jcrysgro.2022.127052
Received 11 July 2022; Received in revised form 13 December 2022; Accepted 16 December 2022

temperature gradient. The sample was not moved, and melting and solidification were solely induced by changing the corresponding temperatures. Similar results have been reported in the literature [9–12]. However, these studies investigated the microstructural dynamics that occur when the growth of well-developed dendrites stops. Nguyen-Thi et al. [9] performed real-time analysis of temperature gradient zone melting (TGZM) by synchrotron X-ray radiography. A thorough characterisation of both the initial solid during the thermal stabilisation phase prior to solidification (static TGZM) in Al–3.5 wt% Ni alloy and the dendritic microstructure in the later stage of solidification in Al–7.0 wt% Si alloy was accomplished. Using a similar technique, the mushy zone evolution from dendrites to a planar front that occurs when pulling stops was studied for an Al-5 wt% Cu alloy [10]. A detailed analysis of the phenomena is presented in a separate study [11]. The present study capitalizes on the knowledge (as confirmed by the aforementioned studies) that individual droplets migrate by the TGZM at the same velocity as the secondary-side arms. In addition, a gradual increase in the concentration at the macroscopic solid/liquid (s/l) interface and a corresponding interface recoil has also been demonstrated [11]. The phase-field approach used in Ref. [11] was reported in a study by Boussinot et al., wherein a reduced diffusivity in the interdendritic liquid was suggested [12].

A hyper-peritectic Al-18at% Ni alloy and a peritectic Al-25at.%Ni alloy were processed by directional melting/solidification in [13–15]. During the directional melting of the hyper-peritectic alloy, the authors observed three stages: (i) the end of melting without thermal stabilisation; (ii) the transient state during the thermal stabilisation stage, where Ni depletion in the liquid at the initial solid–liquid interface front and the interface recoiled owing to TGZM; and (iii) the final state when the mushy zone transformed into a full solid [13]. During the directional solidification of the corresponding peritectic Al-25at. %Ni alloy, they found an incomplete coverage of peritectic phase on the surface of the primary phase [15]. Below the peritectic temperature, in the presence of incomplete coverage, melting of the primary phase on one side and solidification to the peritectic phase on the other side proceeded swiftly via diffusion through the interphase liquid layer.

2. Experimental

In this study, the experimental procedure comprised four steps, whereby the sample remained immobile and only the temperature conditions were varied. Images and temperature measurements were recorded every 30 s. First, the sample was placed in a cold Bridgman furnace for 14 min. Subsequently, the temperature gradient was activated and maintained constant for 78 min. According to the temperature measurements performed in the hot and cold zones, it took approximately 10 min to establish $T_{\text{hot}} = 428$ K and $T_{\text{cold}} = 365$ K. With a 7 mm adiabatic gap, the temperature gradient can be roughly estimated to be $G \approx 9$ K/mm. However, it is well known that the temperature distribution within the adiabatic gap is not strictly linear, but can be described by a sigmoid function that is governed by an apriori unknown length scale that represents the approximate gap width. Depending on the length scale, the actual gradient can be steeper or flatter.

After a holding period of 78 min, the temperatures of both the hot and cold zones were reduced by approximately 5 K and kept constant for 167 min. The temperature reduction took approximately 2 min on the hot and 8–10 min on the cold side. Finally, the temperatures of the hot and cold zones were increased back to the former values and then kept constant for 19 h. This time, the temperature changes also took approximately 2 min on the hot and 8–10 min on the cold side.

The organic compounds used in the present study were supplied as powders with purities of 99.9+% for TRIS and 99 % for NPG. As NPG is highly hygroscopic, an additional drying process of 24 h at 378 K was performed to reduce the water content. TRIS was used as received. The alloy was manufactured in an inert gas atmosphere by mixing powders of both organic substances in a container and fusing them in the liquid state. The container was sealed during the process because of the low vapour pressure of the NPG. After cooling the melt to room temperature (298.15 K), the alloy was ground to millimetre-sized parts. Sample preparation was performed by filling a rectangular glass cartridge (2000 µm × 100 µm inner dimension, 100 µm wall thickness) with capillary force. The cartridge was placed on a heater, and a small amount of the mixture was melted close to the front side of the cartridge. As soon as the material melted, the alloy was automatically drawn into the cartridge. Finally, the cartridge was sealed with a standard ultraviolet-sensitive glue.

The experiment was performed in a vertical Bridgman furnace fixed on the stage of a Zeiss microscope. The main parts of the furnace comprised two ceramic shells, each covering a brass block. One block served as the hot zone and the other served as the cold zone. In addition, they were separated by an adiabatic gap of 7 mm. The temperature inside the brass parts was controlled using electrically resistive heating elements and a Pt 100 temperature sensor. A sample was drawn through the furnace via a slot in the brass blocks, which is 2.5 mm × 0.5 mm in

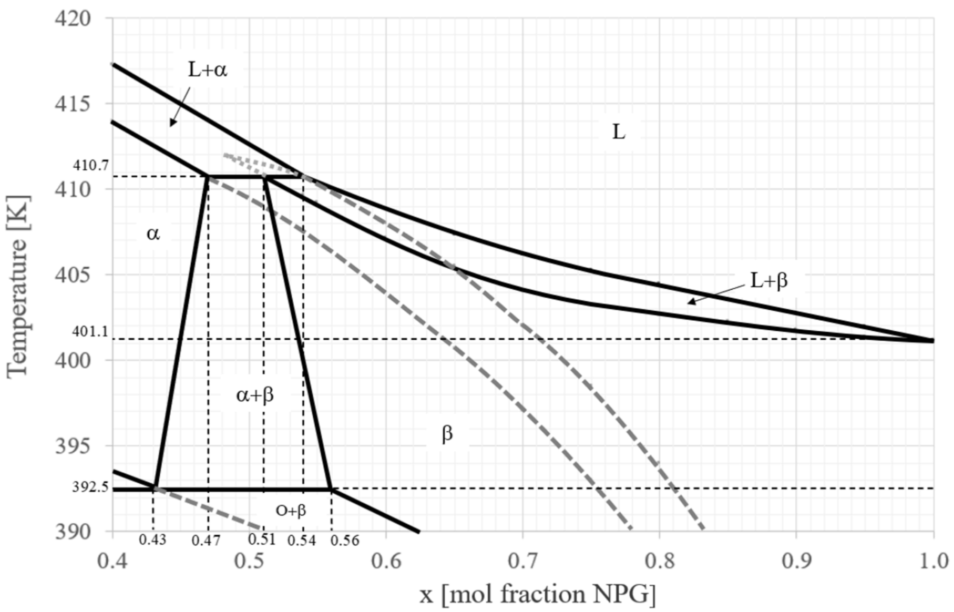

Fig. 1. Relevant part of the Tris(hydroxymethyl) aminomethane–Neopentylglycol (TRIS–NPG) phase diagram according to the measurements by Barrio et al. [4], completed with the metastable extension of the α- and β-liquidus and solidus lines according to the CALPHAD dataset presented herein. The peritectic and the high-temperature eutectoid invariants are specified together with the melting point of the β-phase when containing 100% NPG. The phase regions are labelled based on the equilibrium diagram.

size. The adiabatic zone was illuminated through glass windows in the ceramic plates such that the phenomena inside could be observed using a Zeiss microscope combined with a charge-coupled device camera.

3. CALPHAD modelling

To interpret the present experiment, it is essential to have information on the metastable extensions of the α- and β-liquidus and solidus lines. A thermodynamic description of the TRIS–NPG system is available in the literature [5]. However, the best possible reproduction of high-temperature experimental data, from Barrio et al. [4], is the focus here. Based on published data [5,16,17], the thermodynamic description was re-optimised.

For the pure TRIS compound, the functions of temperature, *T*, which are dependent on the Gibbs energy of the occurring phases, were adopted from Shi et al. [5,16].

$$G_{\mathrm{TRIS}}^{\alpha=\mathrm{bcc}}(T)=H_{\mathrm{TRIS}}^{\mathrm{RT}}+\begin{cases}5412.81-0.2845T^2\\ -2.538\cdot10^{-4}T^3+1.52\cdot10^{-7}T^4\,\mathrm{for}\,10\mathrm{K}<T<\ 445.4\mathrm{K}\\ 54631.46+257.25T-1.821T^2\\ +0.00179T^3-8.553\cdot10^{-7}T^4\,\mathrm{for}\,445.4\mathrm{K}<T<\ 600\mathrm{K}\end{cases}\tag{1}$$

$$G_{\mathrm{TRIS}}^{L}(T)=H_{\mathrm{TRIS}}^{\mathrm{RT}}+\begin{cases}8779.81-7.56T-0.2845T^2\\ -2.538\cdot10^{-4}T^3+1.52\cdot10^{-7}T^4\,\mathrm{for}\,10\mathrm{K}<T<\ 445.4\mathrm{K}\\ 57998.46+249.69T-1.821T^2\\ +0.00179T^3-8.5533\cdot10^{-7}T^4\,\mathrm{for}\,445.4\mathrm{K}<T<600\mathrm{K}\end{cases}\tag{2}$$

$G_{\mathrm{TRIS}}^{\mathrm{O}=\mathrm{ortho}}(T)=H_{\mathrm{TRIS}}^{\mathrm{RT}}+G_{\mathrm{TRIS}}^{\mathrm{SER}}(T)$ with

$$G_{\mathrm{TRIS}}^{\mathrm{SER}}(T)=\begin{cases}-9096.72+18.65T-0.3729T^2\\ +1.912\cdot10^{-4}T^3-1.561\cdot10^{-7}T^4\ \text{for 10 K} < T <\ 445.4\ \mathrm{K}\\ 4600+76898.99-15.05T-1.0559T^2\\ +0.00114T^3-6.4742\cdot10^{-7}T^4\ \text{for 445.4 K} < T <\ 600\ \mathrm{K}\end{cases}\tag{3}$$

The functions for the phases occurring in the pure NPG compound were adopted from Witusiewicz et al. [17].

$$G_{\mathrm{NPG}}^{\beta=\mathrm{fcc}}(T)=H_{\mathrm{NPG}}^{\mathrm{RT}}+\begin{cases}-26046.6841+8.04112T-0.368865T^2\\ -1.883333\cdot10^{-4}T^3+2.3294167\cdot10^{-7}T^4\ \text{for 10 K} < T <\ 403\ \mathrm{K}\\ -16498.0451-66.312676T-0.16873T^2\\ -3.916667\cdot10^{-4}T^3+2.79216667\cdot10^{-7}T^4\ \text{for 403 K} < T <\ 600\ \mathrm{K}\end{cases}\tag{4}$$

$$G_{\mathrm{NPG}}^{L}(T)=H_{\mathrm{NPG}}^{\mathrm{RT}}-23251.4835+5.6221T-0.39224T^2\\ -1.3166667\cdot10^{-4}T^3+1.6645\cdot10^{-7}T^3\tag{5}$$

$G_{\mathrm{NPG}}^{\mathrm{M}\,=\,\mathrm{mono}}(T)=H_{\mathrm{NPG}}^{\mathrm{RT}}+G_{\mathrm{NPG}}^{\mathrm{SER}}(T)$ with

$$G_{\mathrm{NPG}}^{\mathrm{SER}}(T)=\begin{cases}-27892.88-0.439805T^2\\ +3.445\cdot10^{-4}T^3-2.9885\cdot10^{-7}T^4\ \text{for 10 K} < T <\ 314.5\ \mathrm{K}\\ -13655.397-160.56542T+0.225275T^2\\ -8.483333\cdot10^{-4}T^3+4.78225\cdot10^{-7}T^4\ \text{for 314.5 K} < T <\ 600\ \mathrm{K}\end{cases}\tag{6}$$

Here, $H_{\mathrm{TRIS}}^{\mathrm{RT}}$ and $H_{\mathrm{NPG}}^{\mathrm{RT}}$ are the enthalpies of formation of pure TRIS and pure NPG, respectively, in their standard element reference (SER) states at room temperature (298.15 K) and 1 bar pressure. All data are presented in SI units.

The expressions for the hypothetical (metastable) pure TRIS phases, $G_{\mathrm{TRIS}}^{\beta}$ and $G_{\mathrm{TRIS}}^{\mathrm{M}}$, and the hypothetical (metastable) pure NPG phases, $G_{\mathrm{NPG}}^{\alpha}$ and $G_{\mathrm{NPG}}^{\mathrm{O}}$, are as follows:

$$G_{\mathrm{TRIS}}^{\beta}(T)=G_{\mathrm{TRIS}}^{\alpha}(T)+H_{\mathrm{TRIS}}^{\mathrm{RT}}+1600\tag{7}$$

$$G_{\mathrm{TRIS}}^{\mathrm{M}}(T)=G_{\mathrm{TRIS}}^{\mathrm{SER}}(T)+H_{\mathrm{TRIS}}^{\mathrm{RT}}+7889.2\tag{8}$$

$$G_{\mathrm{NPG}}^{\alpha}(T)=G_{\mathrm{NPG}}^{\beta}(T)+H_{\mathrm{NPG}}^{\mathrm{RT}}+354.94\tag{9}$$

$$G_{\mathrm{NPG}}^{\mathrm{O}}(T)=G_{\mathrm{NPG}}^{\mathrm{SER}}(T)+H_{\mathrm{NPG}}^{\mathrm{RT}}+4600\tag{10}$$

In a binary system A–B (e.g. TRIS–NPG), the Gibbs energy expression for solution-phase $\phi=\alpha,\beta,\mathrm{O},\mathrm{M}$ and L is usually expressed as

$$G^{\phi}(T,x)=x_{\mathrm{A}}G_{\mathrm{A}}^{\phi}(T)+x_{\mathrm{B}}G_{\mathrm{B}}^{\phi}(T)+RT[x_{\mathrm{A}}\ln(x_B)+x_{\mathrm{B}}\ln(x_{\mathrm{B}})]+G^{\mathrm{EX},\phi}(T,x)\tag{11}$$

with $x_{\mathrm{A}}=x$ and $x_{\mathrm{B}}\ =1-x$

$$G^{\mathrm{EX},\phi}(T,x)=x_{\mathrm{A}}x_{\mathrm{B}}(L_0^{\phi}(T)+L_1^{\phi}(T)(x_{\mathrm{A}}-x_{\mathrm{B}}))\tag{12}$$

The interaction parameters for the different TRIS–NPG phases were obtained by re-optimising the thermodynamic description such that the experimental values of Barrio et al. [4] for the peritectic, the two eutectoids and the melting point of pure NPG were reproduced up to the third digit. re-optimisation was conducted using the PARROT data optimisation module integrated in the Thermo-Calc software package.[1]

$$L_0^{\alpha}(T)=14830-30.5888T\ \mathit{and}\ L_1^{\alpha}(T)=1916.2-5.835T\tag{13}$$

$$L_0^{\beta}(T)=13803.8-34.1854T\ \mathit{and}\ L_1^{\beta}(T)=-32682.8+85.8083T\tag{14}$$

$$L_0^{L}(T)=20414.9-43.1740T\ \mathit{and}\ L_1^{L}(T)=-325.4\tag{15}$$

$$L_0^{\mathrm{O}}(T)=10237.8-14.4812T\ \mathit{and}\ L_1^{\mathrm{O}}(T)=-661.7\tag{16}$$

$$L_0^{\mathrm{M}}(T)=3983.7\ \mathit{and}\ L_1^{\mathrm{M}}(T)=0\tag{17}$$

Fig. 2 shows the resulting stable and metastable TRIS–NPG phase diagrams in comparison with the measurements from Barrio et al. [4]. If nucleation hindrance makes the formation of the β phase difficult, then the α-phase forms solid solutions over the full concentration range (Fig. 2b). The (metastable) melting point of the bcc α-phase that comprises 100 % NPG is predicted to be at $T_{f,\mathrm{NPG}}^{\alpha}=369.1$ K. In the case of no β phase formation, the high-temperature eutectoid (α ↔ β + O), at $T_{e1}=392.5$ K and $x_{e1}=0.437$ mol fraction NPG, disappears and the two-phase region (α + O) spreads all the way down to the new eutectoid invariant reaction (α ↔ O + M) at $T_{e2'}=322.9$ K and $x_{e2'}=0.983$ mol fraction NPG. It is also important to mention that the metastable solidification interval of the α-phase gradually widens for higher NPG compositions. If no α-phase forms (Fig. 2c), then the metastable β-phase melts congruently ($T_c=411.6$ K at $x_c=0.465$ mol fraction NPG). Moreover, metastable β-phase participates in a new eutectic invariant reaction, L ↔ β + O, at $T_{e3'}=401.5$ K and $x_{e3'}=0.287$ mol fraction NPG.

---

[1] https://thermocalc.com/products/thermo-calc/.

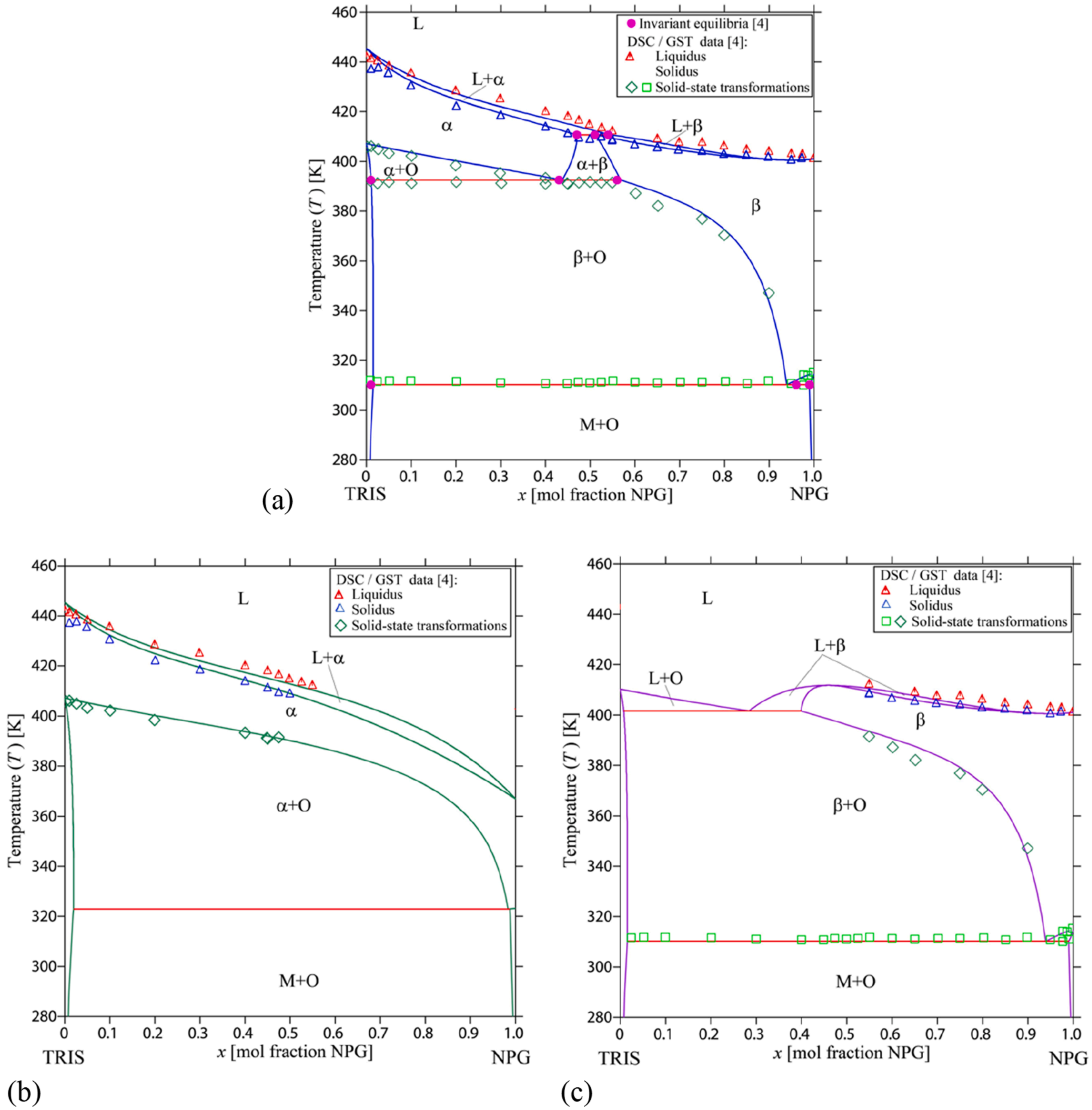

Fig. 2. Stable (a) and metastable (b and c) TRIS–NPG phase diagrams as obtained with the dataset defined by Eqs. (1)–(17). The β-phase has been suspended for (b) and the α-phase has been suspended for (c).

4. Experimental results

The challenge of the present experimental observations is to distinguish between the two ODICs (α and β) and the liquid, as they are optically indistinguishable. To distinguish between the different phases, their dynamic behaviour based on the TRIS–NPG phase diagram can be utilised. Shortly after placing the just-filled hot sample into the cold Bridgman furnace, spherulitic and faceted crystals nucleated and grew into large irregular grains of a transparent and plastic phase until the entire sample was filled with these spherulites. Within minutes after the gradient was activated, the samples showed (i) spherulites on the cold side, (ii) liquid on the hot side, and (iii) a fine-grained structure in between.

Fig. 3a1 shows the microstructure after the temperature gradient had been fully established, and Fig. 3a2 shows the microstructure 60 min later. During this period, the grain boundaries gradually migrated from the cold to the hot zone, while the grains became increasingly coarse. In addition, the solid/liquid (s/l) interface moved to lower temperatures. Subsequently, after reducing the temperature levels on both sides of the samples by approximate 5 K, the grain boundaries became clearly thinner and the s/l interface shot rapidly forward by forming fine dendrites. These fine dendrites immediately began to coarsen and gradually transformed back into a planar front. Fig. 3b1 shows this dendrite coarsening stage and the fine dendrites in the inset. The faceted crystals on the low-temperature side of the sample required more time to adapt to the new temperature field. However, after 152 min, they were fully established, as shown in Fig. 3b2. From the distance at which the dendrite tips grew forward and the distance at which the faceted crystals evolved, temperature gradients of approximately 11 K/mm for the hot side and 9 K/mm for the cold side could be determined. Note that the

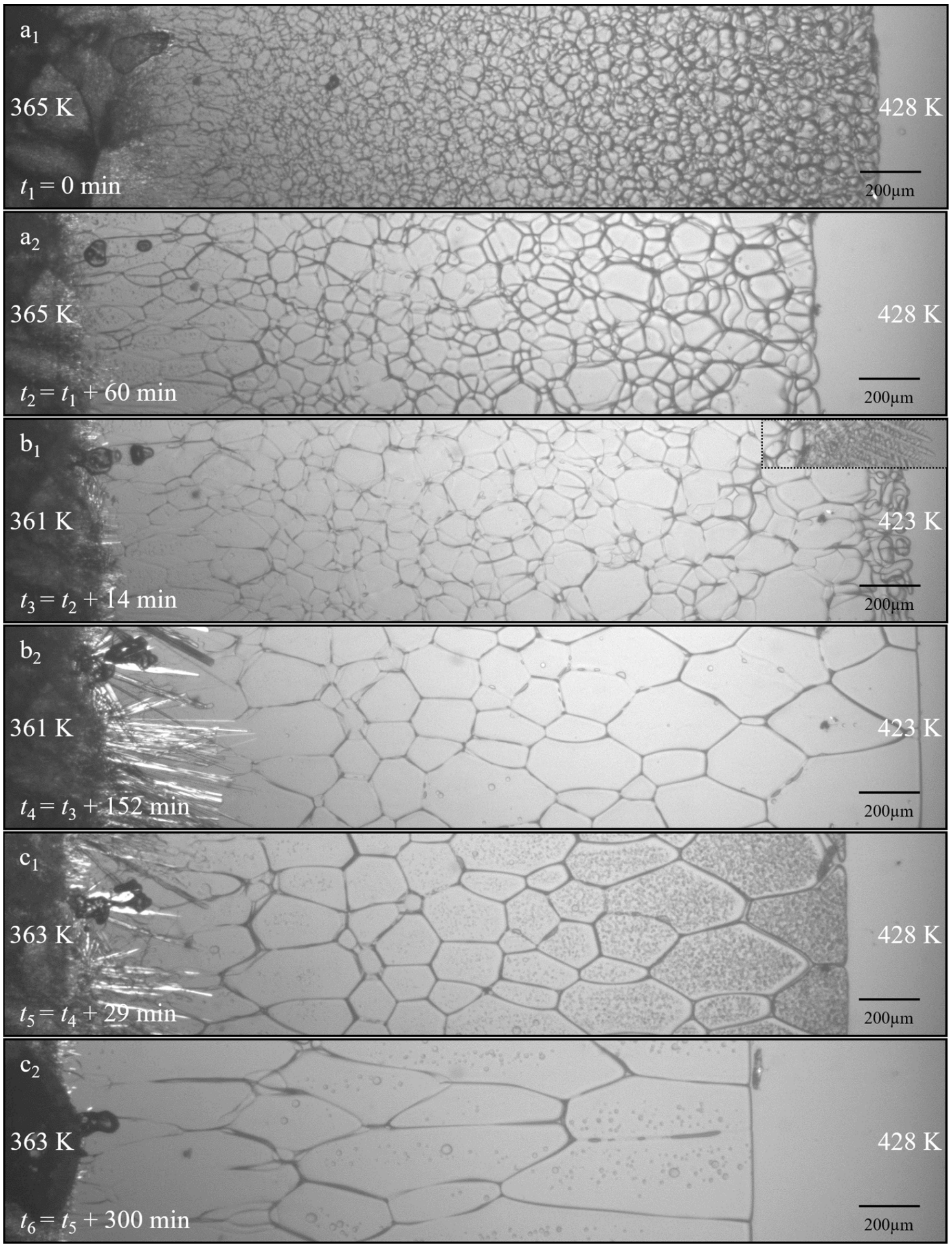

Fig. 3. Microstructures (a_1) after thermal equilibration with $T_{\text{hot}} = 428$ K, $T_{\text{cold}} = 365$ K, (a_2) 60 min later, (b_1) another 14 min later after thermal equilibration with $T_{\text{hot}} = 423$ K, $T_{\text{cold}} = 361$ K, (b_2) 152 min later, (c_1) another 29 min later after thermal equilibration with $T_{\text{hot}} = 428$ K, $T_{\text{cold}} = 363$ K, (c_2) 300 min later. The given temperatures are those that have been measured at the hot and cold zones. They are not exactly present at the image edges as the images show only 3.09 mm from the 7 mm wide adiabatic gap. (A supplementary video is available at https://doi.org/10.1016/j.jcrysgro.2022.127052.).

foremost tips of the faceted crystals are not located on a clear isotherm. Thus, the estimated cold-side gradient has a slight degree of vagueness.

When the temperatures were increased back to the former levels, (i) the s/l interface moved to a lower position, (ii) the grain boundaries became wider, and (iii) the grains were covered with many spots - less spots at low temperatures and more spots at high temperatures (Fig. 3c1). From the magnified observations, it is clear that these spots comprised liquid droplets. Together with the grain boundaries, these droplets migrated from cold to hot, and droplet-free layers formed at the leading edge of the grains. By waiting sufficiently long, nearly all the droplets migrated to the s/l interface, whereby the interface continued to move to lower positions. Fig. 3c2 shows the microstructure approximately 330 min after the temperature level was increased back to the former values. Unintentionally, a macroscopic bubble formed in the low-temperature part of the sample, which can be partly observed on the left side of Fig. 3c2.

According to the phase diagram in Fig. 1, the temperature on the left side of Fig. 3a1, a2, c1, and c2 must be assumed to be below $T_{e1} = 392.5$ K (when the faceted two-phase region is assumed to comprise O + β) or below 390 K (when it comprises O + α). The temperature on the right side must be assumed to be above the liquidus temperature of the present alloy, $T_l = 412.7$ K for $c_0 = 0.5$ mol fraction NPG. For Fig. 3b1 and b2, the left-side temperature is 4 K and the right-side temperature is 5 K lower than those mentioned above.

To estimate the migration velocity of the grain boundaries and liquid droplets located in the solid, the displacement in the longitudinal direction was analysed as a function of time. For this, Fig. 3b1 and c1 were compared to an image taken 900 s later, and Fig. 3b2 and c2 were compared to an image taken 900 s earlier. This choice ensured an equal temperature distribution and expected displacements on the order of 100–400 µm, which is sufficiently large for good optical cognition. Fig. 3a1 cannot be evaluated with sufficient accuracy because grain coarsening is the main driving force for grain boundary migration, and the alteration of the microstructure is too dynamic.

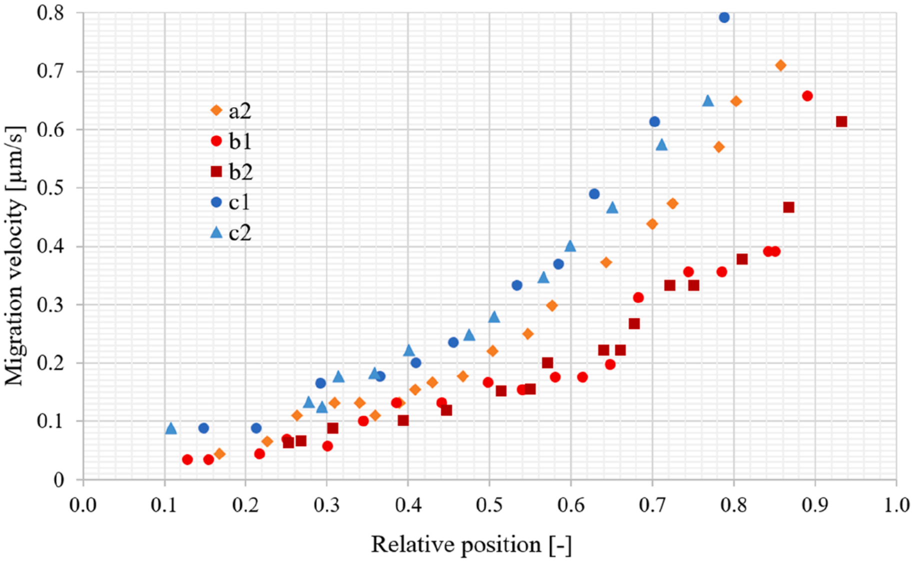

Fig. 4. Measured migration velocities for Fig. 3**a2, b1, b2, c1, and c2** as a function of the relative position within the images (left side: 0, right side: 1).

Fig. 4 shows the migration velocities estimated for Fig. 3a2, b1, b2, c1, and c2. As no reliable temperature information along the sample axis is available, the values have been plotted as a function of the relative position (left side: 0, right side: 1). Evidently, grain boundary migration happens over the whole temperature range from around T_{e1} (left side) to around T_l (right side). Close to the low-temperature boundary T_{e1}, the migration velocities are quite small but are detectable. Conversely, close to the s/l interface, around T_l, they are remarkably high. The migration curves from Fig. 3b1 and b2 are similar. The same can be stated for those from Fig. 3c1 and c2. Meanwhile, the c-curves are remarkably different from the b-curves. This difference becomes smaller when shifting the b-curves by 0.13 of the relative position to the left. The b-curves have been estimated at a ~ 5 K different temperature level, which results in temperature displacement by ~ 500 µm for the cold side and 450 µm for the hot side. This displacement corresponds to ~ 0.13 of the relative position for the cold and ~ 0.12 for the hot side.

Furthermore, it is interesting to mention that most of the grain boundaries seen in Fig. 3a1, b1, and c1 reached the s/l interface within the corresponding holding time and thus disappeared in Fig. 3a2, b2, and c2, respectively. It can be concluded from Fig. 4 that the grain boundaries shown in Fig. 3**a** migrate within 60 min by ~ 160 µm at lower temperatures and by ~ 2600 µm at higher temperatures. For Fig. 3b, ~320 and ~ 5900 µm were estimated for a holding time of 152 min, and for Fig. 3c, ~1600 and ~ 14.000 µm were estimated for 300 min. The width of the images in Fig. 3 is 3090 µm.

5. Discussion

In light of the TRIS–NPG phase diagram (Fig. 1), it must be assumed that the area with faceted crystals, that can be seen on the left side of the images in Fig. 3, comprises a two-phase mixture of either O + β or O + α. When comparing the evolution of this area with time, it becomes evident that the faceted O-phase needs time to adapt to changing conditions. For example, by reducing the temperature by ~ 5 K, it took more than 60 min to approach the final position of the O-phase needles (Fig. 3b2). When the temperature was increased back to the former value, it took more than 2 h for the O-phase needles to completely dissolve (Fig. 3c2).

Nevertheless, as previously stated, the temperature on the left side of Fig. 3 can be assumed to be below $T_{e1} = 392.5$ K (when the faceted two-phase region is assumed to comprise O + β) or below 390 K (when it comprises O + α). The temperature on the right side is above the liquidus temperature of the present alloy, $T_l = 412.7$ K for $c_0 =$ 0.5 mol fraction NPG. Of utmost importance is the fact that according to the TRIS-NPG phase diagram (Fig. 1), a Scheil-type solidification of the peritectic β-phase would always terminate at $T_{f,\mathrm{NPG}} = 401.1$ K, that is, the melting point of pure NPG. Below 401.1 K, the peritectic β-phase cannot be in equilibrium with any TRIS-NPG liquid. Therefore, if a solid/liquid mixture is observed at temperatures lower than the $T_{f,\mathrm{NPG}}$, the corresponding solid can only be in the (metastable) properitectic α-phase. Above $T_{f,\mathrm{NPG}}$, grains that comprise β or are at least incompletely covered by β, as reported in [15], might be in equilibrium with intergranular liquid. However, the problem with this hypothesis is that when β exists at higher temperatures, it would definitely spread down along the grain boundaries until it reaches the low-temperature limit at T_{e1} and thus, a solid/liquid mixture below $T_{f,\mathrm{NPG}}$ would disappear. Because we have clearly observed liquid grain boundaries close to T_{e1}, it can be concluded that the peritectic β-phase must be absent during the experiment presented in this study.

Pioneering studies by Pfann [18], Tiller [19] and Allen and Hunt [20] showed that under certain conditions, a liquid inclusion, either in the form of a droplet or a channel, can migrate through a solid by imposing a stationary temperature gradient across the solid. This phenomenon is called temperature-gradient zone melting (TGZM). The opposite sides of the liquid inclusion are at different temperatures; therefore, they have a different solute composition, as thermodynamic equilibrium holds at each interface. Hence, there is a solute gradient across the inclusion, and the solute diffuses from one side to the other (from the cold side to the hot side for the TRIS–NPG alloys). This causes solidification on the cold side and melting on the hot side, so that the droplet migrates up the temperature gradient. Tiller suggested that the migration velocity be obtained using a simple flux balance:

$$V_{\mathrm{mig}} = \frac{-GD_l}{mC_l^*(1-k)} = \frac{-GD_l}{\Delta T_0(C_l^*)} \tag{18}$$

where G is the temperature gradient, D_l is the diffusion coefficient in the liquid, m is the liquidus slope, k is the redistribution coefficient, and C_l^* is the concentration on the liquid side of the solidifying interface. The denominator of Eq. (18) represents the solidification interval, ΔT_0, at C_l^*. Principally, Eq. (18) can be applied to a liquid droplet but also to a 'wet' grain boundary. When the 'wet' grain boundary is inclined with respect to the temperature gradient, only the component perpendicular to the temperature gradient will migrate according to Eq. (18).

As suggested by Watson and Hunt [21] the experimental measurement of the migration velocities of droplets during TGMZ can be used to estimate the often-unknown diffusion coefficient when phase diagram and temperature gradient are known. Liu et al. estimated D_l for dilute Succinonitrile (SCN)-salol and SCN-Camphor transparent alloys by applying TGZM investigations [22]. They measured the traces of individual droplets migrating from afar to close proximity relative to the s/l interface. As they studied dilute alloys, they assumed that D_l does not change with temperature or concentration, despite the fact that the droplet concentration gradually decreases when approaching the s/l-interface. The same method was applied by one of the present authors (JM) in his Ph.D. thesis by using alloys from TRIS-NPG [23]. Diffusion coefficients in the order of $D_l \cong 3 \times 10^{-5}$ mm^2/s are suggested. However, for non-dilute alloys, the assumption of a concentration-independent diffusion coefficient that is valid for the entire droplet trajectory is vague. In case of TRIS-NPG with $c_0 = 0.5$ mol fraction NPG, the concentration within a droplet (or 'wet' grain boundary) changes from 0.82 mol fraction NPG (at $T_{e1} = 392.5$ K) to 0.5 mol fraction NPG (at $T_l = 412.7$ K). Therefore, for non-dilute alloys, an incremental rather than an integral evaluation of the droplet migration is advised.

In the present case, we obtain (by applying Eq. (18)) $D_l \cong 2.7 \times 10^{-5}$ mm^2/s for the low temperature positions and $D_l \cong 2.4 \times 10^{-4}$ mm^2/s for the high temperature positions based on the phase diagram information for the metastable α-phase shown in Fig. 1 and the measured migration velocities shown in Fig. 4. For the temperature gradient, we assumed $G = 10$ K/mm to obtain these D_l values. As G is only roughly known, the above diffusion coefficients are not cut in stone. In addition, it cannot be decided whether the increase inD_l, by a factor of approximately 10, is due to the temperature increase, concentration reduction, or both. Furthermore, according to Fig. 1, the ΔT_0 for β is less than half that for α and tends to zero when approaching 412 K and 401 K. Thus, D_l would be more than double for a certain range and would show a singularity at these two temperatures. Such unrealistic scenarios can also be used to exclude the presence of the β-phase.

Boussinot et al. [12] applied the Arrhenius law to describe the reduction in diffusion in the interdendritic liquid at lower temperatures. For Al-4wt.%Cu they considered a 40 % reduction from T_l to around $0.9T_l$. Clearly, this is not as drastic as the case presented here. However, Al-4wt.%Cu can still be considered dilute compared to the present non-dilute alloy. Kamgar et al. recently reported measured mutual diffusion coefficients in non-ideal and concentrated liquid solutions [24]. They collected data for several alcohol-X mixtures, where X represents Benzene, Carbon disulphide, or carbon tetrachloride. Evidently, in inorganic and organic liquid solutions, the diffusion coefficient may frequently change with concentration by a factor of 2–5 even at the same temperature.

The hypothesis that the grains shown in Fig. 3 comprise a supersaturated α-phase is also confirmed by the fact that liquid precipitation occurs within the grains by quickly reducing the temperature level (Fig. 3c1). Furthermore, the corresponding grains reveal a precipitation-free layer at their 'hot' edges. One might intuitively consider that these layers represent the β-phase that incompletely covers the α grains. However, this idea is incorrect. In less than a minute, the temperature of the hot zone increased from 423 K to 428 K (with a small and rapid overshoot of 1 K), whereby the cold zone remained at the same temperature level. This rapid temperature increases in the hot zone resulted in a sudden occurrence of liquid precipitation, as shown in Fig. 5. Apparently, the solid enters the s/l two-phase region when the temperature level is increased, and the solid can now reduce the supersaturation by forming liquid droplets. As shown in Fig. 5b, no precipitation-free layer exists at the instant the precipitation first occurs. However, at a velocity of 0.4 μm/s, a grain boundary migrates a distance of 24 μm in 60 s. This is approximately the thickness of the precipitation-free layer formed during the period between Fig. 5b and c. Thus, the precipitation-free layers form by growth rather than from a different phase.

Whether the grain boundaries migrate differently compared with liquid precipitation has also been investigated. Fig. 6 shows the corresponding magnified region at approximately 0.55–0.6 relative position. The 'colder' droplets (located at the bottom of the image) migrate slower than the 'hotter' ones (located at the top of the image). Both the droplets and grain boundaries migrated at the same velocity depending on the local temperature (and composition). The fact that the precipitated droplet migrated at the same velocity as the grain boundaries justifies the use of Eq. (18) for grain boundary migration and is in accordance with [11,12].

Notably, long-lasting grain boundary migration by TGZM gradually increases the solute content at the s/l interface [11,12]. However, the strength of this recoil depends not only on the migration duration and velocity, but also on the amount of segregated liquid that allows solute diffusion to the s/l interface. Comparing Fig. 3a1 and a2, the interface recoiled by 200 μm in 60 min. Comparing Fig. 3b1 and b2, it did not recoil at all, although 152 min passed between the two images. Here, the grain boundaries become rather thin. Conversely, when the TGZM of

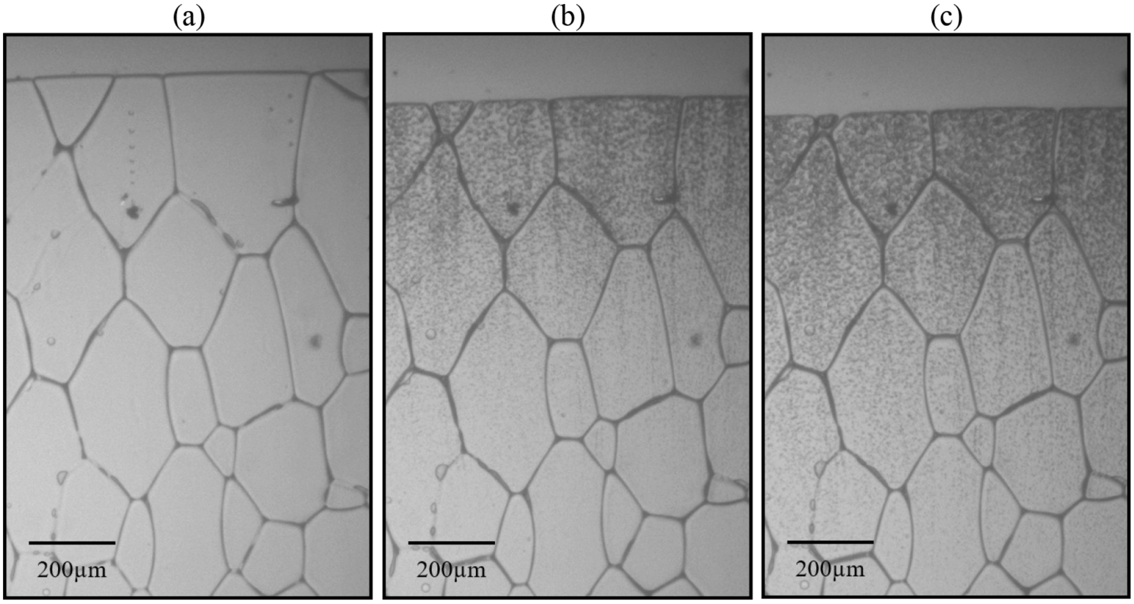

Fig. 5. Effect of a sudden temperature-level increase on the s/l interface and the occurrence of liquid precipitations: (a) initial stage with $T_{\text{hot}} = 423$ K, $T_{\text{cold}} = 361$ K; (b) 60 s later with $T_{\text{hot}} = 429$ K, T_{cold} unchanged; (c) another 60 s later with $T_{\text{hot}} = 428$ K, T_{cold} still unchanged (turned by − 90° compared to that in Fig. 3).

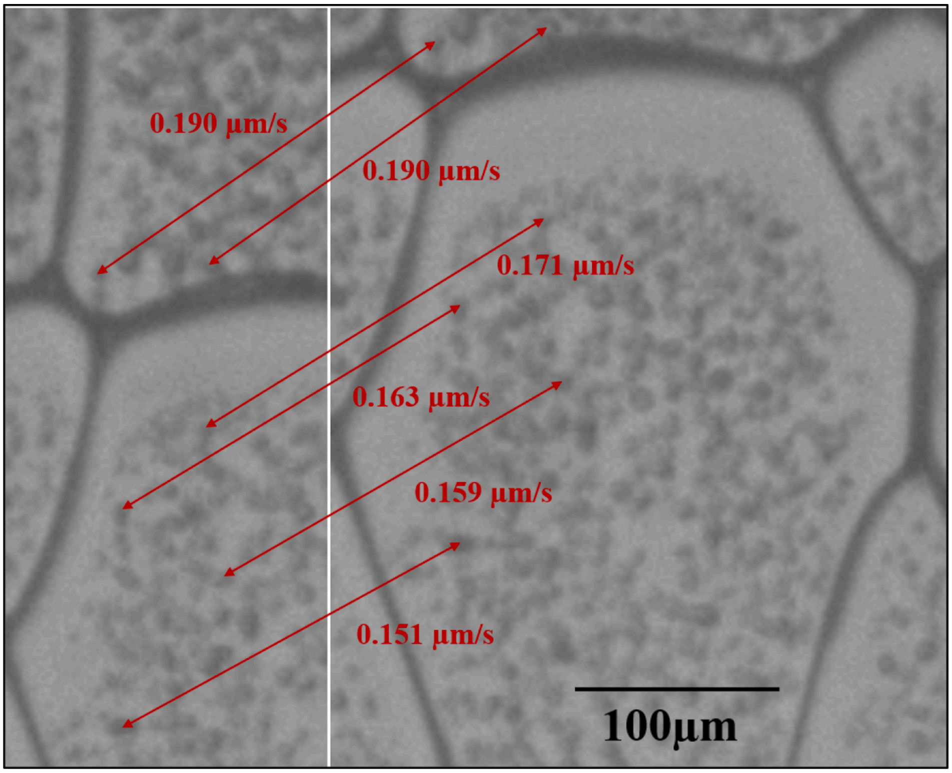

Fig. 6. Magnified images taken at $t_4 + 39$ min (left in half) and at $t_4 + 49$ min (right in full). The two images have been taken at the same position in the sample at ~ 0.6 relative position. Now, the gradient is pointing upwards with hot being on top and cold being below (turned by − 90° compared to that in Fig. 3).

liquid precipitation contributed to an increase in the solute content at the s/l interface, as shown in Fig. 3c1 and c2, the recoil is again stronger. Here, we obtained 312 µm in 300 min.

Generally, by grain coarsening and elongation, the number of grain boundaries that reach the s/l interface decreases with time; hence, the rate at which the solute content at the s/l interface increases also decreases with time. Therefore, the TGZM recoil as a function of time first resembles a root function and later approaches an accumulation point (when no grain boundaries parallel to the isotherms exist anymore).

6. Conclusions

Although thermodynamically predicted, no indication of the presence of a peritectic β-phase was found in the experiments conducted in this study. When the temperature gradient was activated, a fine-grained microstructure comprising a pro-peritectic α-phase surrounded by a liquid was formed. By obtaining the metastable extensions of the α-liquidus and solidus lines from a thermodynamic assessment, we can consider that for the present TRIS–NPG alloy with a 0.5 mol fraction of NPG, the fine grains reveal a segregation profile with a solute-pure core and a solute-rich outer edge that is in contact with an NPG-rich liquid. Thus, the outer edges of the grains were supersaturated. This is the starting point for grain coarsening and grain boundary migration by TGZM.

During the subsequent dynamic processes, the situation evidently changed: In particular, grain boundary migration by TGZM led to an alteration of segregation such that the solute content at the foremost planar s/l interface increased and the interface recoiled to lower temperatures. The grains themselves formed less supersaturated layers at their 'hot' edges owing to resolidification. However, without the β-phase, the growth of the α-phase led to a supersaturated solid, based on the metastable extension of the α-liquidus and solidus.

Local evaluation of the grain boundary migration velocity suggests that the diffusivity of NPG in TRIS-NPG liquids changed from $D_l \cong 2.4 \times 10^{-4}$ mm^2/s for 0.50 mol fraction NPG and $T_l = 412.7$ K to $D_l \cong 2.7 \times 10^{-5}$ mm^2/s for 0.82 mol fraction NPG and $T_{e1} = 392.5$ K. This change might have been caused by both the temperature decrease of $\Delta T = 20$ K and the composition increase by approximately $\Delta c = 40\%$. With a diffusion coefficient that decreases drastically, the diffusion dynamics during the initial transient might differ from the classical view of establishing a steady-state exponential profile, and a longer transition period must be expected.

CRediT authorship contribution statement

A. Ludwig: Conceptualization, Writing – original draft. **J. Mogeritsch:** Investigation. **V.T. Witusiewicz:** .

Declaration of Competing Interest

The authors declare that they have no known competing financial interests or personal relationships that could have appeared to influence the work reported in this paper.

Data availability

Data will be made available on request.

Acknowledgements

This research was supported by the European Space Agency (ESA) in the framework of the project METCOMP and by the Austrian Research Promotion Agency (FFG) under grant number 865969.

Appendix A. Supplementary data

Supplementary data to this article can be found online at https://doi.org/10.1016/j.jcrysgro.2022.127052.

References

[1] H. Feng, X. Liu, S. He, K. Wu, J. Zhang, Studies on solid–solid phase transitions of polyols by infrared spectroscopy, Thermochim. Acta. 348 (2000) 175–179, https://doi.org/10.1016/s0040-6031(99)00403-7.

[2] S. Santos-Moreno, S. Doppiu, G.A. Lopez, N. Marinova, Á. Serrano, E. Silveira, E. P. del Barrio, Study of the phase transitions in the binary system NPG-TRIS for thermal energy storage applications, Materials (Basel). 13 (2020) 1–22, https://doi.org/10.3390/ma13051162.

[3] N. De La Pinta, S. Santos-Moreno, S. Doppiu, J.M. Igartua, E. Palomo Del Barrio, G. A. López, Npg–tris thermal storage system. Quantification of the limiting processes: Sublimation and water's adsorption, Crystals. 11 (2021), https://doi.org/10.3390/cryst11101200.

[4] M. Barrio, D.O. Lopez, J.L. Tamarit, P. Negrier, Y. Haget, Degree of miscibility between non-isomorphous plastic phases: Binary system NPG (neopentyl glycol)-TRIS [tris(hydroxymethyl)aminom, J. Mater. Chem. 5 (1995) 431–439, https://doi.org/10.1039/JM9950500431.

[5] R. Shi, D. Chandra, A. Mishra, A. Talekar, M. Tirumala, D.J. Nelson, Thermodynamic reassessment of the novel solid-state thermal energy storage materials: Ternary polyalcohol and amine system pentaglycerine-tris (hydroxymethyl)-amino-methane-neopentylglycol (PG-TRIS-NPG), Calphad. 59 (2017) 61–75, https://doi.org/10.1016/j.calphad.2017.08.003.

[6] A. Ludwig, J. Mogeritsch, M. Rettenmayr, On/off directional solidification of near peritectic TRIS-NPG with a planar but tilted solid/liquid interface under microgravity conditions, Scr. Mater. 214 (2022), 114683, https://doi.org/10.1016/j.scriptamat.2022.114683.

[7] A. Ludwig, J. Mogeritsch, Observation of peritectic couple growth for a hyper-peritectic alloy under micrograviry conditions, in: IOP Conf. Ser. Mater. Sci. Eng., 2022: p. in print.

[8] J. Mogeritsch, W. Sillekens, A. Ludwig, In-situ Observation of Coupled Growth Morphologies in Organic Peritectics under Pure Diffusion Conditions, in: Miner. Met. Mater. Ser. B. Ser., 2022: pp. 1429–1441. 10.1007/978-3-030-92381-5_136.

[9] H. Nguyen-Thi, G. Reinhart, A. Buffet, T. Schenk, N. Mangelinck-Noel, H. Jung, N. Bergeon, B. Billia, J. Härtwig, J. Baruchel, In situ and real-time analysis of TGZM phenomena by synchrotron X-ray radiography, J. Cryst. Growth. 310 (2008) 2906–2914, https://doi.org/10.1016/j.jcrysgro.2008.01.041.

[10] G. Salloum-Abou-Jaoude, G. Reinhart, H. Combeau, M. Založnik, T.A. Lafford, H. Nguyen-Thi, Quantitative analysis by in situ synchrotron X-ray radiography of the evolution of the mushy zone in a fixed temperature gradient, J. Cryst. Growth. 411 (2015) 88–95, https://doi.org/10.1016/j.jcrysgro.2014.10.053.

[11] A.B. Phillion, M. Založnik, I. Spindler, N. Pinter, C.A. Aledo, G. Salloum-Abou-Jaoude, H. Nguyen Thi, G. Reinhart, G. Boussinot, M. Apel, H. Combeau, Evolution of a mushy zone in a static temperature gradient using a volume average approach, Acta Mater. 141 (2017) 206–216, https://doi.org/10.1016/j.actamat.2017.09.011.

[12] G. Boussinot, M. Apel, Phase field and analytical study of mushy zone solidification in a static thermal gradient: From dendrites to planar front, Acta Mater. 122 (2017) 310–321, https://doi.org/10.1016/j.actamat.2016.09.053.

[13] Y. Su, D. Liu, X. Li, L. Luo, J. Guo, H. Fu, Preparation of the initial solidliquid interface and melt in directional solidification of Al18 at%Ni peritectic alloy, J. Cryst. Growth. 312 (2010) 2441–2448, https://doi.org/10.1016/j.jcrysgro.2010.05.018.

[14] D. Liu, X. Li, Y. Su, L. Luo, B. Zhang, R. Chen, J. Guo, H. Fu, An analysis of non-equilibrium peritectic reaction driven by solute diffusion under a temperature gradient, J. Cryst. Growth. 334 (2011) 195–199, https://doi.org/10.1016/j.jcrysgro.2011.08.034.

[15] D. Liu, X. Li, Y. Su, M. Rettenmayr, J. Guo, H. Fu, Local melting/solidification during peritectic solidification in a steep temperature gradient: Analysis of a directionally solidified Al-25at%Ni, Appl. Phys. A. 116 (2014) 1821–1831, https://doi.org/10.1007/s00339-014-8336-0.

[16] R. Shi, I. Gantan, D. Chandra, W.M. Chien, A. Talekar, A. Mishra, J. Wang, M. Tirumala, D.J. Nelson, Thermodynamic assessment of binary systems Tris (hydroxymethyl)aminomethane-Pentaglycerine (TRIS-PG) and 2-amino-2-methyl-1,3-propanediol-Pentaglycerine (AMPL-PG) phase diagrams, Calphad. 52 (2016) 264–273, https://doi.org/10.1016/j.calphad.2016.01.006.

[17] V.T. Witusiewicz, L. Sturz, U. Hecht, S. Rex, Thermodynamic description and unidirectional solidification of eutectic organic alloys: II. (CH3)2C(CH2OH) 2-(NH2)(CH3)C(CH2OH)2 system, Acta Mater. 52 (2004) 5071–5081. 10.1016/j.actamat.2004.07.013.

[18] W.G. Pfann, Temperature gradient zone melting, AIME 203 (1955) 961–964, https://doi.org/10.1007/BF03377594.

[19] W.A. Tiller, Migration of a liquid zone through a solid, J. Appl. Phys. 34 (1963) 2757–2769, https://doi.org/10.1063/1.1729806.

[20] D.J. Allen, J.D. Hunt, Temperature gradient zone melting and microsegregation in castings, in: Int. Conf. Solidif. Cast. 1. London Inst. Met., 1977: pp. 39–43.

[21] M.P. Watson, J.D. Hunt, Measurement of liquid diffusion coefficients in the Al-Cu system using temperature gradient zone melting, Met. Trans A. 8 (1977) 1793–1798, https://doi.org/10.1007/BF02646884.

[22] S. Liu, J. Teng, J.Y. Choi, Determination of the Solute Diffusion Coefficient by the Droplet Migration Method, Met. Mater. Trans. A. 38 (2007) 1555–1562, https://doi.org/10.1007/s11661-007-9164-z.

[23] J. Mogeritsch, Investigation on peritectic solidification using a transparent organic system, Ph.D. Thesis, Montanuniversitaet Leoben, AUT, 2012.

[24] A. Kamgar, N. Hamedi, S. Mohsenpour, M.R. Rahimpour, Investigation of using different thermodynamic models on prediction ability of mutual diffusion coefficient model, J. Mol. Liq. 243 (2017) 781–789, https://doi.org/10.1016/j.molliq.2017.08.069.